Progress In Electromagnetics Research, Vol. 123, 509–526, 2012

PLANAR GRATING MULTIPLEXERS USING SILICON NANOWIRE TECHNOLOGY: NUMERICAL SIMULATIONS AND FABRICATIONS

J. Song[1,*], Y. Li[1], X. Zhou[1], and X. Li[2]

[1]Key Lab of Optoelectronics Devices and Systems of Ministry of Education/Guangdong Province, Institute of Optoelectronics, Shenzhen University, Shenzhen 518060, China

[2]Science College, Hangzhou Normal University, Hangzhou, Zhejiang 310036, China

Abstract—Planar waveguide gratings have shown great potential for the application of the wavelength division multiplexing (WDM) functionality in optical communications due to their compactness and high spectral finesse. Planar gratings based on silicon nanowire technology have high light confinements and consequently very high integration density, which is 1–2 orders of magnitude smaller than conventional silica based devices. In the present paper, we will simulate the silicon nanowire based planar grating multiplexer with total-internal-reflection facets using a boundary integral method. The polarization dependent characteristics of the device are analyzed. In addition, the planar grating multiplexer with 1 nm spacing is fabricated and characterized. Compared with measured values, the numerical results show that the sidewall roughness in the grating facets can result in a large insertion loss for the device.

1. INTRODUCTION

Fiber-optic communication is growing extensively in recent years [1–3]. Nowadays a great number of optical fibers have been laid on all parts of the world, which dramatically increases the capacity and the quality of telecommunications. However, traditional optical fibers are still inadequate to carry the heavy traffic resulted from the exponential increase of the bandwidth demand. Fortunately, the wavelength division multiplexing (WDM) technique [4–6] provides an effective and

Received 4 November 2011, Accepted 29 December 2011, Scheduled 6 January 2012

* Corresponding author: Jun Song (songjun@szu.edu.cn).

low-cost way to increase the capacity tens or hundreds of times in an optical transmission system.

Optical multiplexers are the key components in a WDM fiber-optical communication system. A cost-effective scheme for carrying more information can be implemented by inserting them on both sides of a fiber link. Many technologies can be used for multiplexers. Multiplexers based on planar integrated optical waveguides [7, 8] take the advantages of mature semiconductor manufacturing process and can offer more than 40 channels of dense wavelength division multiplexing (DWDM) with a relatively low loss. Among them, the arrayed waveguide grating (AWG) [9] is the most famous one. Compared with an AWG, a planar grating multiplexer [10] is more compact and potentially has a higher spectral finesse since it can accommodate a larger number of grating facets. These characteristics make the planar grating multiplexer more suitable for communication systems of high channel density.

Different technologies based on different materials have been introduced to support planar optical devices. Silica-on-silicon technology has been widely adopted for fabrications of WDM devices in commercial systems. However, a common drawback of the silica-based photonic integrated devices is the overall size of components, mostly limited by the large bending radius. To increase the integration density for future WDM systems a considerable size reduction is necessary. To stay with silicon, as it is the most popular material for modern micro-electronics, silicon based nanowire waveguides were introduced, formed as silicon strips on a silica layer. A very high contrast of refractive index in all directions allows for high light confinement and consequently very high integration density [11–14].

Due to its simplicity in obtaining, e.g., the passband width, a scalar diffraction method based on the Huygens principle of secondary wavelets has become a popular technique for the simulation of a planar grating multiplexer [15]. We have designed and fabricated the grating multiplexers based on both echelle [16] and total internal reflection (TIR) facets [17] using the silicon nanowire technology. However, there always exists a large performance difference between numerical results with the scalar analysis and measurements. For planar gratings using silicon nanowire platform, the grating facets are relatively so small (close to the wavelength) that the accuracy of the scalar diffraction method is limited in the analysis of the diffraction efficiency. Moreover, the essential polarization dependent characteristics of the diffraction grating cannot be treated with the scalar method. Therefore, one needs a more accurate simulation tool which can take the polarization effects into consideration.

In principle, the finite difference time domain (FDTD) method [18–22] can be used for an accurate simulation. However, it is too time-consuming for simulating a planar grating multiplexer device. On the other hand, the rigorous coupled-wave analysis (RCWA) [23, 24] is an effective numerical method for simulating the polarization-dependent diffraction property from a planar grating. However, RCWA cannot be used to simulate the imaging of a concave grating in the large free propagation region.

In the present paper, we present the first rigorous treatment (using the full electromagnetic theory of light) of planar grating multiplexers. As an example, the polarization dependent characteristics of a planar grating multiplexer are analyzed using the boundary integral method for a dielectric grating with TIR facets. Using the numerical method, main specifications of the device (e.g., loss, polarization dependent loss (PDL), and chromatic dispersion) are analyzed in detail and an insightful physical explanation for the numerical results is also given. In addition, a planar grating multiplexer with TIR facets is also fabricated and characterized.

2. SIMULATION METHOD

A planar grating multiplexer based on a Rowland mounting is illustrated in Figure 1. The field propagating from an input waveguide to the free propagation region (FPR) is diffracted by each grating facet. It is then refocused onto an imaging curve and guided into the corresponding output waveguides according to the wavelengths. The grating of a planar grating multiplexer is usually coated with a metal (e.g., Au) at the backside in order to enhance the reflection efficiency (see Figure 2(a)). In order to reduce the reflection loss without the additional processing steps required for coating the backside of the grating facets with a reflecting metal, a TIR facet was used at each grating tooth (see Figure 2(b)). In this design light hits each grating facet at about 45° incidences producing total internal reflection. Due

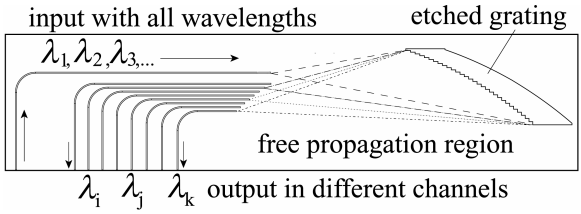

Figure 1. Schematic diagram of a planar grating multiplexer.

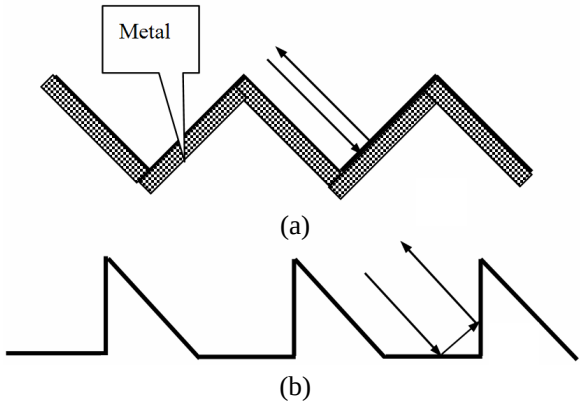

Figure 2. Schematic diagram of (a) an echelle grating and (b) a TIR grating.

to the simple fabrication, we only consider the TIR case in the present paper.

Planar grating multiplexers using silicon nanowire platform typically have sub-wavelength-size grating facets (i.e., ~ 1 micrometer grating period). For an accurate analysis with polarization characteristics solved, we consider the polarization dependent analysis of a finite aperiodic concave grating by using a boundary integral method (BIM) [25–30]. The BIM represents the integral form of the wave equation for each polarization case in terms of the corresponding field distributions on the boundary of the planar grating. Re-radiation field from the surface distributions in turn generates a diffracted field that can be determined anywhere in space. Boundary conditions at a dielectric interface are employed to simplify the resulting equations so that the field distribution can be determined at the dielectric interface using the computer adapted boundary element method. Using the present method, many important performances (such as the PDL, the insertion loss and the chromatic dispersion) for the TIR gratings can be accurately analyzed.

The BIM simulation method can be divided into the following parts:

a) Calculation of the incident field at the grating surface. Since the FPR is homogeneous, the Kirchhoff-Huygens diffraction formula can be used to simulate accurately the propagation of the incident light field in the FPR. Thus, the incident field at a point $P_g(x, z)$ on a grating facet can be calculated with the following integral over the cross-sectional line where the end of the input waveguide is positioned

(hereafter referred as the input plane),

$$E_g(x,z) = \frac{1}{2}\left(\frac{n_{eff}}{\lambda}\right)^{\frac{1}{2}} \int\limits_{\text{input}} \frac{E_{in}(x',z')}{\sqrt{|\overline{P_{in}P_g}|}}(1+\cos\theta_d)e^{-jk|\overline{P_{in}P_g}|}dl \quad (1)$$

where n_{eff} and k are the effective refractive index and wave number in the FPR, respectively, λ is the wavelength in vacuum, E_{in} [representing the electric (or magnetic) field component perpendicular to the chip for the TM (or TE) mode] denotes the fundamental mode field of the input waveguide at the input plane, $|\overline{P_{in}P_g}|$ is the distance between point $P_g\,(x,z)$ and a point $P_{in}\,(x',z')$ on the input plane, and θ_d is the diffraction angle with respect to the normal of the input plane (see Figure 1). Note that TE and TM polarizations are considered separately since different boundary conditions are imposed for different polarizations.

b) Calculation of the re-radiation field (which, in turn, generates a diffracted field) from the surface distribution of the etched grating with a BIM. For the TE (or TM) case, Green's second identity can be used to solve the dielectric boundary problem for the corresponding Helmholtz equation. The solution space is divided into two homogeneous regions: region 1, which is the FPR, and region 2, which contains the planar grating. Thus, one has the following boundary integral equation (which describes the coupling between the scattered field on the grating surface and those in the FPR) for the TE case,

$$\begin{aligned} H_{y1}(\vec{r}) \;=\; & H_g(\vec{r}) + \frac{j}{4}\oint\limits_C \Big[k_1(\vec{n}\cdot\vec{r})\,H_{y1}(\vec{r}')\,H_1^{(2)}\left(k_1|\vec{r}-\vec{r}'|\right) \\ & + H_0^{(2)}\left(k_1|\vec{r}-\vec{r}'|\right)\frac{\partial H_{y1}(\vec{r}')}{\partial n}\Big]dl' \text{ (Region 1)} \end{aligned} \quad (2)$$

and

$$\begin{aligned} H_{y2}(\vec{r}) \;=\; & -\frac{j}{4}\oint\limits_C \Big[k_2(\vec{n}\cdot\vec{r})\,H_{y2}(\vec{r}')\,H_1^{(2)}\left(k_2|\vec{r}-\vec{r}'|\right) \\ & + H_0^{(2)}\left(k_2|\vec{r}-\vec{r}'|\right)\frac{\partial H_{y2}(\vec{r}')}{\partial n}\Big]dl' \text{ (Region 2)} \end{aligned} \quad (3)$$

where $H_g(\vec{r})$ is the incident magnetic field at point $\vec{r}$, $k_1 = 2\pi n_{eff}/\lambda$ and $k_2 = 2\pi n_g/\lambda$, n_g is the refractive index in the etched grating region, $\vec{r}$, $\vec{r}'$ are position vectors of two arbitrary points located on the boundary C, $H_1^{(2)}$ and $H_0^{(2)}$ is the first order and the zero order Hankel function of the second kind, respectively, $H = H_g + H_s$, H_s is the re-radiation magnetic field and $\vec{r} = (\vec{r}-\vec{r}')/|\vec{r}-\vec{r}'|$.

Since the Hankel functions are singular at boundary points where $\vec{r} = \vec{r}'$, the singularities are treated by considering a small circular contour. When the small argument approximations for the relevant Hankel functions are used, Equations (2) and (3) can be expressed as,

$$H_{y1}(\vec{r})\left(\frac{\theta}{2\pi}\right) = H_g(\vec{r}) + \frac{j}{4}\int\limits_{\text{Cauchy}}\left[k_1(\vec{n}\cdot\vec{r})\cdot H_{y1}(\vec{r}')\cdot H_1^{(2)}\left(k_1\left|\vec{r}-\vec{r}'\right|\right) + H_0^{(2)}\left(k_1\left|\vec{r}-\vec{r}'\right|\right)\frac{\partial H_{y1}(\vec{r}')}{\partial n}\right]dl' \text{ (Region 1)} \quad (4)$$

and

$$H_{y2}(\vec{r})\left(1-\frac{\theta}{2\pi}\right) = -\frac{j}{4}\int\limits_{\text{Cauchy}}\left[k_2(\vec{n}\cdot\vec{r})\cdot H_{y2}(\vec{r}')\cdot H_1^{(2)}\left(k_2\left|\vec{r}-\vec{r}'\right|\right) + H_0^{(2)}\left(k_2\left|\vec{r}-\vec{r}'\right|\right)\frac{\partial H_{y2}(\vec{r}')}{\partial n}\right]dl' \text{ (Region 2)} \quad (5)$$

where θ is the angle exterior to region 1.

The boundary condition ($H_{y1} = H_{y2} = H_y$ and $\frac{1}{n_{eff}^2}\frac{\partial H_{y1}}{\partial n} = \frac{1}{n_g^2}\frac{\partial H_{y2}}{\partial n} = \frac{\partial H_y}{\partial n}$) for Equations (4) and (5) can be used, and the integral equations can be expressed as,

$$H_y(\vec{r})\left(\frac{\theta}{2\pi}\right) = H_g(\vec{r}) + \frac{j}{4}\int\limits_{\text{Cauchy}}\left[k_1(\vec{n}\cdot\vec{r})\,H_y(\vec{r}')\,H_1^{(2)}\left(k_1\left|\vec{r}-\vec{r}'\right|\right) + n_{eff}^2 H_0^{(2)}\left(k_1\left|\vec{r}-\vec{r}'\right|\right)\frac{\partial H_y(\vec{r}')}{\partial n}\right]dl' \text{ (Region 1)} \quad (6)$$

and

$$H_y(\vec{r})\left(1-\frac{\theta}{2\pi}\right) = -\frac{j}{4}\int\limits_{\text{Cauchy}}\left[k_2(\vec{n}\cdot\vec{r})\,H_y(\vec{r}')\,H_1^{(2)}\left(k_2\left|\vec{r}-\vec{r}'\right|\right) + n_g^2 H_0^{(2)}\left(k_2\left|\vec{r}-\vec{r}'\right|\right)\frac{\partial H_y(\vec{r}')}{\partial n}\right]dl' \text{ (Region 2)} \quad (7)$$

A boundary element method is applied to Equations (6) and (7) by dividing the integral boundary into N small straight-line segments and the length of the nth segment is S_n. Then, the point co-location method can be used at the same time, which couples every point on the etched grating surface with all the other points on the surface through

the Hankel functions and their normal derivatives.

$$\begin{cases} H_y(r') = \sum\limits_{n=1}^{N} H_{yn} = 1/2 \sum\limits_{n=1}^{N} (H_{yn} + H_{yn+1}) \\ \partial H_y(r')/\partial n = R_y(r') = \sum\limits_{n=1}^{N} R_{yn} = 1/2 \sum\limits_{n=1}^{N} (R_{yn} + R_{yn+1}) \\ \hat{x_n} = 1/2(x_n + x_{n+1}) \\ \hat{y_n} = 1/2(y_n + y_{n+1}) \end{cases} \tag{8}$$

where x_n, x_{n+1}, z_n and z_{n+1} represent adjacent sample points on the etched grating boundary, and $\hat{x_n}$ and $\hat{y_n}$ is the coordinate values at the sample point. By applying the BEM, Equations (6) and (7) can be put in the following form through a $2N \times 2N$ matrix,

$$\begin{bmatrix} Z1_{n,m} & n_{eff}^2 Y1_{n,m} \\ Z2_{n,m} & -n_g^2 Y2_{n,m} \end{bmatrix} \begin{bmatrix} H_{sm} \\ R_{sm} \end{bmatrix} = \begin{bmatrix} H_{gm} \\ 0 \end{bmatrix} \tag{9}$$

where

$$\begin{aligned} Z1_{n,m} &= \left(\frac{\theta_n}{2\pi}\right)\delta_{mn} - \frac{jk_1}{8}\left[S_n\left(\overrightarrow{n_n}\cdot\overrightarrow{r_n}\right)H_1^{(2)}\left(k_1\left|\overrightarrow{r_n}-\overrightarrow{r_m}\right|\right)\right. \\ &\quad \left. + S_{n+1}\left(\overrightarrow{n_{n+1}}\cdot\overrightarrow{r_{n+1}}\right)H_1^{(2)}\left(k_1\left|\overrightarrow{r_{n+1}}-\overrightarrow{r_m}\right|\right)\right] \\ Y1_{n,m} &= -\frac{j}{8}\left[S_n H_0^{(2)}\left(k_1\left|\overrightarrow{r_n}-\overrightarrow{r_m}\right|\right) + S_{n+1}H_0^{(2)}\left(k_1\left|\overrightarrow{r_{n+1}}-\overrightarrow{r_m}\right|\right)\right], \\ Z2_{n,m} &= \left(1-\frac{\theta_n}{2\pi}\right)\delta_{mn} - \frac{jk_2}{8}\left[S_n\left(\overrightarrow{n_n}\cdot\overrightarrow{r_n}\right)H_1^{(2)}\left(k_2\left|\overrightarrow{r_n}-\overrightarrow{r_m}\right|\right)\right. \\ &\quad \left. + S_{n+1}\left(\overrightarrow{n_{n+1}}\cdot\overrightarrow{r_{n+1}}\right)H_1^{(2)}\left(k_2\left|\overrightarrow{r_{n+1}}-\overrightarrow{r_m}\right|\right)\right] \end{aligned}$$

and

$$Y2_{n,m} = -\frac{j}{8}\left[S_n H_0^{(2)}\left(k_2\left|\overrightarrow{r_n}-\overrightarrow{r_m}\right|\right) + S_{n+1}H_0^{(2)}\left(k_2\left|\overrightarrow{r_{n+1}}-\overrightarrow{r_m}\right|\right)\right].$$

Similarly, for the case of TM polarization, a $2N \times 2N$ matrix can be obtained,

$$\begin{bmatrix} Z1_{n,m} & Y1_{n,m} \\ Z2_{n,m} & -Y2_{n,m} \end{bmatrix} \begin{bmatrix} E_{sm} \\ Q_{sm} \end{bmatrix} = \begin{bmatrix} E_{gm} \\ 0 \end{bmatrix} \tag{10}$$

where $Q_{sm} = \partial E_{sm}/\partial n$.

c) Diffraction from the grating to the image plane (along the Rowland circle) according to the wavelength. Once Equations (9) and (10) are solved for H_s and E_s, the diffracted field (produced by

the re-radiation field) at point P_{out} (x'', z'') on the image plane can be calculated with the following explicit formulas,

$$H^d(\vec{r_d}) = \left\{\frac{k\exp\left[-j\left(kr_d+3\pi/4\right)\right]}{\sqrt{8\pi kr_d}}\right\} \sum_{n=1}^{N} S_n H_{sn}\cos\Phi_n \exp[jk\left(x_n\sin\alpha_{\text{diff},0}+z_n\cos\alpha_{\text{diff},0}\right)] \quad (11)$$

for the TE case, or

$$E^d(\vec{r_d}) = \left\{\frac{k_0\sqrt{\varepsilon\mu}\exp\left[-j(kr_d-\pi/4)\right]}{\sqrt{8\pi kr_d}}\right\} \sum_{n=1}^{N} S_n E_{sn}\exp\left[jk\left(x_n\sin\alpha_{\text{diff},0}+z_n\cos\alpha_{\text{diff},0}\right)\right] \quad (12)$$

for the TM case. Here r_d is the distance from the origin to the output waveguide and $\alpha_{\text{diff},0}$ is the diffraction angle. The length of the ith segment is S_i and its center is at point $(x_i,\ y_i)$. For both polarizations, the field distribution $E_{\text{image}}(x', z')$ at the image plane can be obtained by scanning over the surface of the output waveguide using Equations (11) and (12). When the output waveguide is of single-mode, the spectral response for a certain output channel can be approximated with the following overlap integral,

$$I(f_0+\Delta f) = \frac{\left|\int \tilde{E}_{\text{image}}(x'-(x_0'+D_a\Delta f))\tilde{E}^*_{\text{outwg}}(x')dx'\right|^2}{\int\left|E_{\text{out}}(x'-(x_0'+D_a\Delta f))\right|^2 dx'\int\left|E_{\text{inwg}}(x)\right|^2 dx} \quad (13)$$

where E_{outwg} is the mode profile of the output waveguide, and the superscript $*$ denotes a complex conjugate, f_0 and x_0 are the central frequency and the corresponding focusing position, respectively.

The spectral response describes the amplitude response of the device, while the phase response of the device is represented by the chromatic dispersion. Since the group delay [31] can be given by $\tau = -\frac{\lambda^2}{2\pi c}\frac{\partial\Phi}{\partial\lambda}$, the chromatic dispersion can be calculated by,

$$D = \frac{d\tau}{d\lambda} = -\frac{1}{2\pi c}\left[2\lambda\frac{\partial\Phi}{\partial\lambda}+\lambda^2\frac{\partial^2\Phi}{\partial\lambda^2}\right] \quad (14)$$

where c is the velocity of the light in vacuum, and Φ is the phase response determined by the overlap integral $\int E_{out}(\lambda, x')E_0^*(\lambda, x')dx'$. The dispersions can broaden and distort the signal bits (pulses) and ultimately lead to transmission errors. Applying finite differences

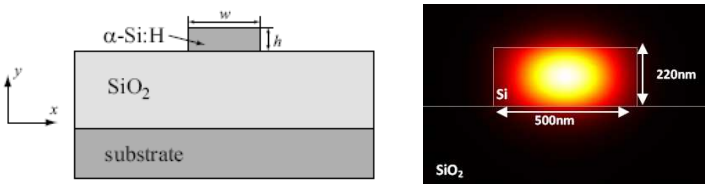

(a) (b)

Figure 3. Sketch of (a) α-silicon nanowire waveguide and (b) the simulated intensity profile of the light in the silicon waveguide.

to Equation (14), the chromatic dispersion D can be calculated numerically as,

$$D_i = \frac{\left(2\lambda\Delta\lambda + \lambda^2\right)\Phi_{\iota+1} - 2\lambda\left(\Delta\lambda + \lambda\right)\Phi_\iota + \lambda^2\Phi_{\iota-1}}{-2\pi c\left(\frac{\Delta\lambda}{\lambda}\right)^2} \tag{15}$$

3. DESIGN AND FABRICATION

The typical structure of a silicon nanowire waveguide based on a silicon substrate is shown in Figure 3(a). The silica buffer layer should be thick enough ($\sim 5\,\mu$m) to ensure a low leaky loss. For a typical photonics application, the thickness $h = 250\,$nm is fixed here, and the width $w = 500\,$nm is chosen, which lies in the single mode region. The intensity profile of the propagating electric field is simulated for the channel wire waveguides (see Figure 3(b)).

To design a planar grating multiplexer, the incident angle and the diffraction order should carefully be selected. The grating center point P_i, the input position I and the center output position O are chosen to be on a circle (called the Rowland circle). The center points P_{i+k} of the other facets on the grating are chosen to be on the second circle (twice the radius of the Rowland circle and tangent to the Rowland circle at point P_i). The fields "reflected" by all grating facets should add in phase so that they are "focused" at one focal point for a designed wavelength λ_0. The center point P_{i+k} is thus determined by the following light path equation,

$$IP_{i+k} + P_{i+k}O - (IP_i + P_iO) = km\lambda_0/n_{eff} \tag{16}$$

With the central points for all the facets determined, the etched grating is constructed by adding the facets at the obtained central points (the k-th facet is the reflective surface for the incident ray IP_k and the reflective ray P_kO).

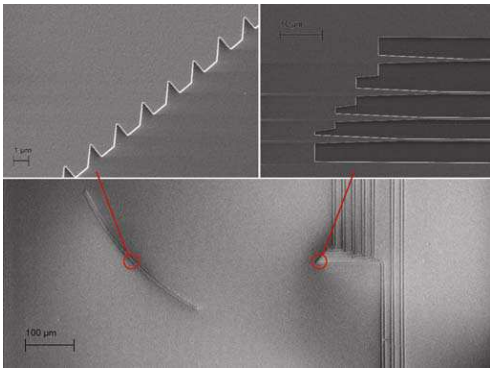

Figure 4. Pictures of the fabricated planar grating multiplexer with TIR facets using silicon nanowire technology.

As an example, a planar grating multiplexer with TIR facets will be designed using the following parameters: the central wavelength is 1550 nm; the refractive indexes of silica buffer layer and α-Si : H core laye are 1.46 and 3.58, respectively; the incident angle is 45 degrees; the diffraction order is 6; channel interval is 1 nm; and the internal of output waveguides is 5 μm.

As the beginning step of the whole device fabrication, a 5 μm silica buffer layer (i.e., SiO_2) and a 220 nm α-Si : H core layer are successively deposited on a silicon wafer. Then a process of pattern generation will be carried out using lithography technology with high resolution and accuracy. In the paper, the electron beam lithography based on negative resists is employed due to its low running cost and ability to push the resolution further down to 50 nm. To increase the coupling efficiency, the width of each input and output waveguide was tapered from 500 nm to 2 μm through a 25 μm long linear taper.

Figure 4 shows one of the fabricated planar grating multiplexers. The roughness of the sidewall (i.e., the side facet of the waveguides and gratings) is $\sim$ 20 nm, which was directly measured from the scanning electron microscopy (SEM) pictures. From this figure, one can see that the dimension of the device is around half millimeter, which is 1–2 orders of magnitude smaller than conventional silica based devices.

4. SIMULATION AND DISCUSSION

Using the same parameters in Section 3, we designed and fabricated an 8-channel planar grating multiplexer. In this work, we employed an end-fire characterization setup to test our devices. An amplified

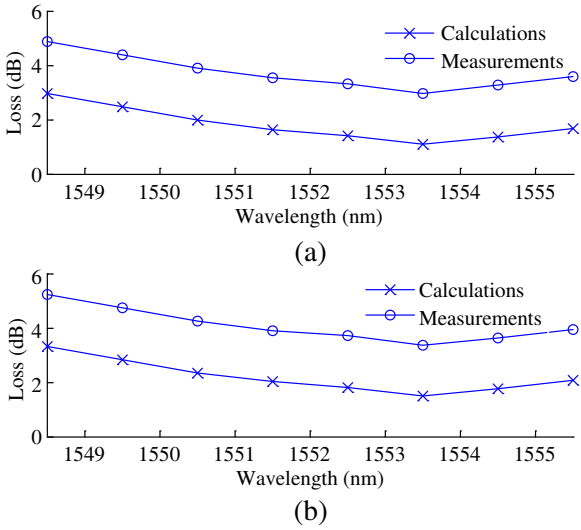

Figure 5. The comparison of the insertion loss of the 8-channel planar grating multiplexer with TIR facets for different wavelength channels (a) for a TE polarization, (b) for a TM polarization.

spontaneous emission source gives a broadband unpolarized light with spectral range 1530 nm–1580 nm. This unpolarized light is butt-coupled to the input waveguide of a component through a focusing gradient index lens. The output light is collected with a microscope objective and split into two beams, one to an infrared camera, and the other to an optical spectrum analyzer through a multi-mode fiber. Polarizers are inserted in front of the infrared camera and the multi-mode fiber in order to separate the two polarizations.

Figure 5 shows the comparison of the insertion loss between measurements and numerical results based on the boundary integral method for both polarizations. From the figure, one can see that the loss of the fabricated device is much higher than that of numerical calculations. We attribute this to the phase error induced in the grating etching, i.e., the grating-facet variation in short range (sidewall roughness) and long range (stability of the E-beam during the pattern writing).

The insertion loss difference between the two polarizations is one of the main reasons for the PDL of the device. To some extent, the fabrication errors have similar influence on the device with different polarizations. Figure 6 shows the comparison of the PDL between measurements and numerical results based on the boundary integral

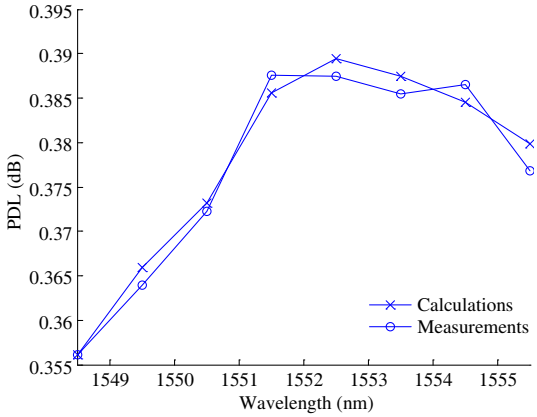

Figure 6. The comparison of the PDL of the 8-channel planar grating multiplexer with TIR facets for different wavelength channels.

method. From this figure, one can see that the measured values agree well in those from numerical calculations. Therefore, the boundary integral method can be accurately used for the analysis of the polarization characteristics of the planar grating multiplexer.

Rough grating sidewalls can be produced in the process of the grating etching, which could result in most of the difference of the loss between calculations and measurements. Now, we will use the boundary integral method to give an analysis for the effect of surface roughness on the loss. One-dimensional Gaussian rough surfaces with Gaussian spectrum [32] are used to model the rough facets of the gratings. The total number of the sampling points on each rough facet is 64. Since Gaussian rough surfaces are independently produced for all grating facets with the same roughness, the numerical results can statistically approach the experimental results. Twenty-one data points for the sidewall roughness (from 0 to 40 nm) and eight data points for λ (from 1548.5 nm to 1555.5 nm) have been used in the following contour plots. The results have not been smoothed in the numerical calculations.

Figure 7 shows the contour plot of the loss for both polarizations as the roughness and the wavelength vary. One can see from this figure that the loss monotonically increases with the sidewall roughness of the facets for both polarizations. Note that the sidewall roughness of the measured device in Figures 5 and 6 is $\sim$ 20 nm (directly measured from the SEM pictures). From Figure 7, we know that the $\sim$ 20 nm roughness can produce about 1.6 dB excess losses for both polarizations in the operating wavelength range, which is very close to the difference

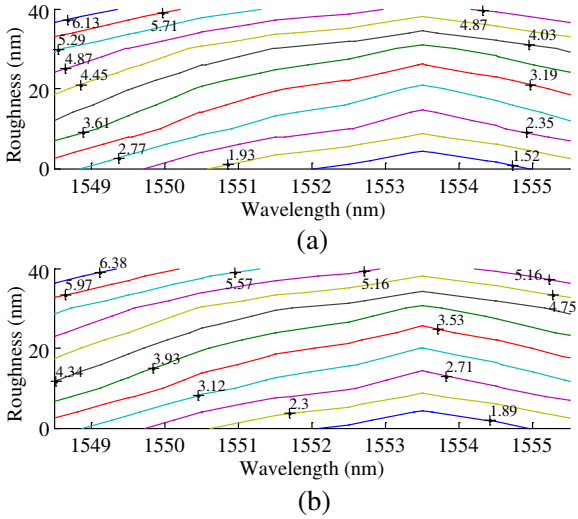

Figure 7. Contour plot of the loss as the sidewall roughness and λ vary for a planar grating multiplexer for (a) TE and (b) TM polarizations.

between numerical results and measured values shown in Figure 5 (i.e., ~ 1.9 dB). The extra loss (e.g., ~ 0.3 dB) could result from the unstable fabrication process of the E-beam during the pattern writing.

The dispersions can broaden and distort the signal bits (pulses) and ultimately lead to transmission errors. When a TIR occurs, a phase distortion occurs because the reflection coefficient is a complex number. Since the boundary integral method takes into account all phase changes, it can also be used to calculate the chromatic dispersion based on Equation (14). Figure 8 shows the calculated chromatic dispersion near the central channel for the planar grating multiplexer with a TIR groove type. From this figure one can see that the TM polarization has a larger dispersion than the TE polarization within the passband. The polarization dependent chromatic dispersion is mainly due to the difference in the type and magnitude of the re-radiation fields on the surface of the planar TIR grating. The re-radiation fields are of electric and magnetic types for the TE and TM cases, respectively.

For a TIR type planar grating multiplexer, the TIR occurs twice when the incident light impinges on an illuminated facet. Though intuitively no loss can be produced when a TIR occurs, our numerical calculations have shown that the loss of a TIR type device is still very large for the silicon nanowire device (cf., Figure 5). An important

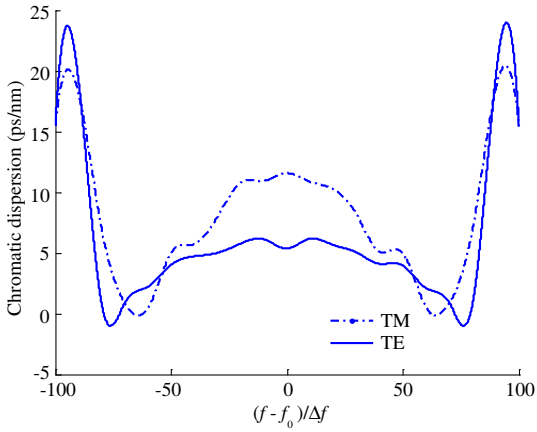

Figure 8. Chromatic dispersion characteristics near the central channel of the designed planar grating multiplexer.

phenomenon related to the total internal reflection is the Goos-Hänchen shift. Physically the Goos-Hänchen shift results from the phase change of the electromagnetic field. We consider that the shift results in the large loss of the TIR-device. From Figure 2(b), one can know that for any incident light impinging on the first facet of a TIR grating; it can not be reflected by the second facet if the distance between its incident point and the right-angle trough point is less than its corresponding Goos-Hänchen shift. For a given incident angle, the Goos-Hänchen shift is a fixed value. Therefore, if the grating period is much larger than the value of the Goos-Hänchen shift, the GH shift will have little effect on the loss of the device. However, the grating period is close to 1 micrometer for the present silicon nanowire device, and then a large loss is inevitable.

For a straight periodic blazed grating, the grating period can be expressed as,

$$\Lambda \approx m\lambda / (2n_{eff} \sin \alpha_{in}) \tag{17}$$

For the planar grating multiplexer, by selecting a large diffraction order one can acquire larger grating facets, which are advantageous in reducing the loss from the shift. In addition, large grating facets can reduce the manufacturing difficulty. However, a large diffraction order can also increase the chip size, obviously. Therefore, one has to select an appropriate diffraction order in the design process, in order to make a compromise between the physical size and the insertion loss.

5. CONCLUSION

In the present paper, we have applied a boundary integral method to the simulation of a planar grating multiplexer based on silicon nanowire platform and gave a semi-vectorial analysis of the finite and aperiodic device. Using the present method, many important characteristics (such as the PDL, the insertion loss and the chromatic dispersion) for the planar grating multiplexer can be accurately analyzed. Numerical results have shown that the sidewall roughness can result in a large loss for the device. Moreover, some physical insights have been discussed on the origin of the diffraction loss in the TIR facets. The designed device is fabricated using a silicon nanowire technology. Measurements agreed well with numerical results.

ACKNOWLEDGMENT

Parts of our works are supported by the National Natural Science Foundation of China (No. 61007032); Natural Science Foundation of Guangdong Province, China (No. 10451806001005352); Special Foundation for Young Scientists of Guangdong Province, China (No. LYM10115) and Scientific Research Foundation for the Returned Overseas Chinese Scholars, State Education Ministry, China.

REFERENCES

1. Fu, X., C. Cui, and S.-C. Chan, "Optically injected semiconductor laser for photonic microwave frequency mixing in radio-over-fiber," *Journal of Electromagnetic Waves and Applications*, Vol. 24, No. 7, 849–860, 2010.
2. Wu, C.-J., T.-J. Yang, and S.-J. Chang, "Analysis of tunable multiple-filtering property in a photonic crystal containing strongly extrinsic semiconductor," *Journal of Electromagnetic Waves and Applications*, Vol. 25, Nos. 14–15, 2089–2099, 2011.
3. Chen, D., G. Hu, X. A. Liu, B. Peng, and G. Wu, "Bending analysis of a dual-core photonic crystal fiber," *Progress In Electromagnetics Research*, Vol. 120, 293–307, 2011.
4. Li, B. and W. Wu, "Compact dual-band branch-line coupler with 20 : 1 power dividing ratio," *Journal of Electromagnetic Waves and Applications*, Vol. 25, No. 4, 607–615, 2011.
5. Lee, H. K., H. J. Lee, and C. H. Lee, "A simple and color-free WDM-passive optical network using spectrum-sliced Fabry-Perot

laser diodes," *IEEE Photonics Technology Letters*, Vol. 20, 220–224, 2008.

6. Melle, S., R. Dodd, and S. Grubb, "Bandwidth virtualization enables long-haul WDM transport of 40 Gb/s and 100 Gb/s services," *IEEE Communications Magazine*, Vol. 46, S22–S29, 2008.
7. Costanzo, S., "Synthesis of multi-step coplanar waveguide-to-microstrip transition," *Progress In Electromagnetics Research*, Vol. 113, 111–126, 2011.
8. Kuo, C.-W., S.-Y. Chen, Y.-D. Wu, and M.-H. Chen, "Analyzing the multilayer optical planar waveguides with double-negative metamaterial," *Progress In Electromagnetics Research*, Vol. 110, 163–178, 2010.
9. Lu, H. C. and W. S. Wang, "Cyclic arrayed waveguide grating devices with flat-top passband and uniform spectral response," *IEEE Photonics Technology Letters*, Vol. 20, 3–5, 2008.
10. Tolstikhin, V. I., A. Demsmore, and K. Pimonov, "Monolithically integrated optical channel monitor for DWDM transmission systems," *Journal of Lightwave Technology*, Vol. 22, 146–153, 2004.
11. Gao, S. M., Z. Q. Li, and X. Z. Zhang, "Power-attenuated optimization for four-wave mixing-based wavelength conversion in silicon nanowire waveguides," *Journal of Electromagnetic Waves and Applications*, Vol. 24, Nos. 8–9, 1255–1265, 2010.
12. Wu, J.-J. and B.-R. Shi, "Frequency response of silicon-clad proton-exchanged channel waveguides," *Journal of Electromagnetic Waves and Applications*, Vol. 25, Nos. 5–6, 651–659, 2011.
13. Zhao, W.-S., X.-P. Wang, and W.-Y. Yin, "Electrothermal effects in high density through silicon via (TSV) arrays," *Progress In Electromagnetics Research*, Vol. 115, 223–242, 2011.
14. Butt, H., Q. Dai, T. D. Wilkinson, and G. A. J. Amaratunga, "Photonic crystals & metamaterial filters based on 2D arrays of silicon nanopillars," *Progress In Electromagnetics Research*, Vol. 113, 179–194, 2011.
15. He, J. J., E. S. Koteles, and B. Lamontagne, "Integrated polarization compensator for WDM waveguide demultiplexers," *IEEE Photonics Technology Letters*, Vol. 11, 224–226, 1999.
16. Song, J. and N. Zhu, "Design and fabrication of compact etched diffraction grating demultiplexers based on α-Si nanowire technology," *Electronics Letters*, Vol. 44, 816–817, 2008.

17. Song, J. and J. F. Ding, "Amorphous-Si-based planar grating demultiplexers with total internal reflection grooves," *Electronics Letters*, Vol. 45, 905–906, 2009.
18. Tay, W. C. and E. L. Tan, "Implementations of PMC and PEC boundary conditions for efficient fundamental ADI and LOD-FDTD," *Journal of Electromagnetic Waves and Applications*, Vol. 24, No. 4, 565–573, 2010.
19. Pu, T.-L., K.-M. Huang, B. Wang, and Y. Yang, "Application of micro-genetic algorithm to the design of matched high gain patch antenna with zero-refractive-index metamaterial lens," *Journal of Electromagnetic Waves and Applications*, Vol. 24, Nos. 8–9, 1207–1217, 2010.
20. Zhang, Z. and W. Dou, "Binary diffractive small lens array for THz imaging system," *Journal of Electromagnetic Waves and Applications*, Vol. 25, Nos. 2–3, 177–187, 2011.
21. Dou, W., "Analysis of THz imaging system with a refractive small lens array by a hybrid numerical method," *Journal of Electromagnetic Waves and Applications*, Vol. 25, Nos. 8–9, 1317–1328, 2011.
22. Bicer, M. B., A. Akdagli, and A. Kayabasi, "Simple formulas for calculating resonant frequencies of C and H shaped compact microstrip antennas obtained by using artificial Bee colony algorithm," *Journal of Electromagnetic Waves and Applications*, Vol. 25, Nos. 11–12, 1718–1729, 2011.
23. Jarem, J. M., "Rigorous coupled wave analysis of bipolar cylindrical systems: Scattering from inhomogeneous dielectric material, eccentric, composite circular cylinders," *Progress In Electromagnetics Research*, Vol. 43, 181–237, 2003.
24. Lalanne, P., "Highly improved convergence of the coupled-wave method for TM polarization," *J. Opt. Soc. Am. A*, Vol. 13, 779–784, 1996.
25. Petit, R., *Electromagnetic Theory of Gratings*, Springer-Verlag, Berlin, 1980.
26. Collino, F., F. Millot, and S. Pernet, "Boundary-integral methods for iterative solution of scattering problems with variable impedance surface condition," *Progress In Electromagnetics Research*, Vol. 80, 1–28, 2008.
27. Valagiannopoulos, C. A., "A novel methodology for estimating the permittivity of a specimen rod at low radio frequencies," *Journal of Electromagnetic Waves and Applications*, Vol. 24, Nos. 5–6, 631–640, 2010.

28. Wang, A.-Q., L.-X. Guo, and C. Chai, "Numerical simulations of electromagnetic scattering from 2D rough surface: Geometric modeling by Nurbs surface," *Journal of Electromagnetic Waves and Applications*, Vol. 24, No. 10, 1315–1328, 2010.
29. Cui, Z.-W., Y.-P. Han, and M.-L. Li, "Solution of CFIE-JMCFIE using parallel MoM for scattering by dielectrically coated conducting bodies," *Journal of Electromagnetic Waves and Applications*, Vol. 25, Nos. 2–3, 211–222, 2011.
30. Lai, B., H.-B. Yuan, and C.-H. Liang, "Analysis of Nurbs surfaces modeled geometries with higher-order MoM based aim," *Journal of Electromagnetic Waves and Applications*, Vol. 25, Nos. 5–6, 683–691, 2011.
31. Kikuchi, N., "Adaptive chromatic dispersion compensation using higher order polarization-mode dispersion," *IEEE Photonics Technology Letters*, Vol. 13, 1115–1117, 2001.
32. Tsang, L., J. A. Kong, and K. H. Ding, *Scattering of Electromagnetic Waves (Volume I: Theories and Applications)*, John Wiley & Sons, 2000.